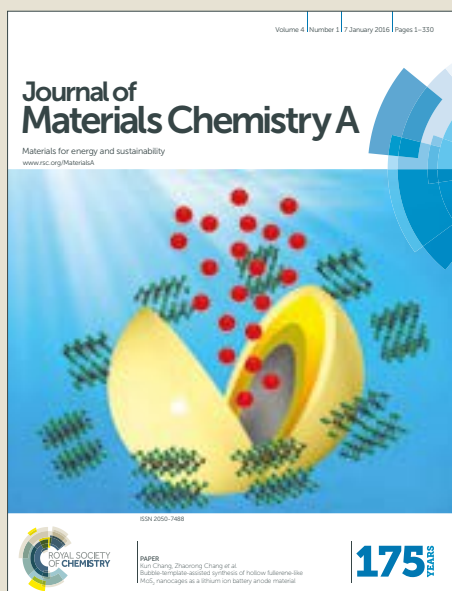


Journal of Materials Chemistry A

Accepted Manuscript



This article can be cited before page numbers have been issued, to do this please use: Y. Li, L. Liu, Y. Wu, T. Wu, H. Wu, Q. Cai, Y. Xu, B. Zeng, C. Yuan and L. Dai, *J. Mater. Chem. A*, 2019, DOI: 10.1039/C9TA00890J.

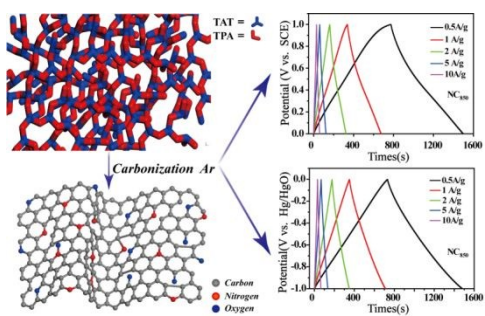


This is an Accepted Manuscript, which has been through the Royal Society of Chemistry peer review process and has been accepted for publication.

Accepted Manuscripts are published online shortly after acceptance, before technical editing, formatting and proof reading. Using this free service, authors can make their results available to the community, in citable form, before we publish the edited article. We will replace this Accepted Manuscript with the edited and formatted Advance Article as soon as it is available.

You can find more information about Accepted Manuscripts in the [author guidelines](#).

Please note that technical editing may introduce minor changes to the text and/or graphics, which may alter content. The journal's standard [Terms & Conditions](#) and the ethical guidelines, outlined in our [author and reviewer resource centre](#), still apply. In no event shall the Royal Society of Chemistry be held responsible for any errors or omissions in this Accepted Manuscript or any consequences arising from the use of any information it contains.



Hierarchical porous nitrogen-doped carbon materials possess an outstanding supercapacitance performance in both acid and alkaline electrolytes.



Journal Name

ARTICLE

Facile Synthesis of Nitrogen-Doped Carbon Materials with Hierarchical Porous Structures for High-Performance Supercapacitors in Both Acid and Alkaline Electrolytes

Received 00th January 20xx,
Accepted 00th January 20xx

DOI: 10.1039/x0xx00000x

www.rsc.org/

Yuntong Li, Ling Liu, Yuzhe Wu, Tong Wu, Haiyang Wu, Qipeng Cai, Yiting Xu, Birong Zeng, Conghui Yuan* and Lizong Dai*

In this report, we show that a facile and highly adaptable route based on the Schiff-base formation reaction, can generate crosslinked polymer precursors for the fabrication of hierarchical porous nitrogen-doped carbon materials. The optimized sample with moderate surface wettability, Brunauer-Emmett-Teller (BET) area, heteroatom content displays outstanding supercapacitance performances in both acid and alkaline electrolytes. The capacitances of 362 F g⁻¹ in 1 M H₂SO₄ and 374.5 F g⁻¹ in 6 M KOH at 0.5 A g⁻¹ as well as excellent rate capability (75% and 79.5% capacitance retention at 30 A g⁻¹ in 1 M H₂SO₄ and 6 M KOH, respectively) can be achieved, which are much better than that of the sample fabricated via conventional synthetic route (acetic acid as catalyst). Moreover, by the differing slopes of the discharge portion, electric double layer capacitors (EDLC) and faradaic capacitance contributions to the overall specific capacitance are analyzed. It is found that the faradaic capacitance is mainly associated with heteroatom content and the available utilization of heteroatom. The EDLC capacitance is related to the BET surface area, surface wettability, the concentration and ionic size of the electrolyte. This simple synthetic strategy may be of interest in the design of crosslinked polymer precursors, thus fabricating carbon materials with unique electrochemical properties. Moreover, our finding of EDLC and faradaic capacitance contributions to the overall specific capacitance is crucial for the future fabrication of nitrogen-doped carbons in supercapacitors.

Introduction

With the intensification of global energy crisis, exploring clean, sustainable and high performance energy materials is of particularly importance for the development of energy conversion and storage devices.^{1,2} Pure carbon materials, such as activated carbon, carbon black, graphene and carbon nanotube have attracted considerable attention for their attractive properties including large surface area, high electrical conductivity, excellent chemical stability.³⁻⁶ As supercapacitor electrode materials, carbon materials can be used as both cathodes and anodes, and reversibly operated in a fairly large electrochemical window. However, their low energy storage ability (150~200 F g⁻¹, based on the weight of the active materials), which is limited by the physical charge storage mechanism of electric double layer capacitors (EDLC), severely impedes their commercial application.⁷⁻¹⁰ Therefore, fabrication of carbon-based materials with promising structures/composites, such as surface area, pore size distribution, heteroatom content, surface functionality, has

become a major research focus, thus achieving excellent overall specific capacitance (EDLC and faradaic capacitances).

So far, a crowd of heteroatoms (e.g., B, N, P, S) have been applied to dope carbon materials for elevating their capacitance performance. Among them, nitrogen-doped carbon materials have attracted intensive attention due to their increased conductivity, improved wettability and capacitive performance in comparison with pure carbon materials. This is because more electrons are brought to the delocalized π -system of carbon materials and the density of states at the Fermi level is increased when electron-rich nitrogen atoms are introduced into the carbon network. Moreover, doping of nitrogen offers additional faradaic capacitance to pure carbon materials, while preserving its excellent intrinsic characteristics.^{1,6,11-14}

Nitrogen-doped carbon materials are usually obtained from two approaches: i) directly heating treatment of carbon matrix and inorganic nitrogen compounds, such as ammonia, urea. Nevertheless, this method is difficult to control the uniformity and component of the carbon materials, due to the poor compatibility between nitrogen sources and carbon materials. Besides, the inclusion nitrogen content is relatively low since it prefers to generate nitrogen functionalities on the surface rather than the actual nitrogen-doping into the carbon matrix.^{1,15-17} ii) direct pyrolysis of nitrogen-containing precursors, like polyaniline, polypyrrole, polyacrylonitrile, metal organic frameworks (MOFs) and covalent triazine-based frameworks (CTFs).^{1,5,8,18-22} Recently, covalent organic

Fujian Provincial Key Laboratory of Fire Retardant Materials, College of Materials, Xiamen University, Xiamen, 361005, China. E-mail : *yuanch@xmu.edu.cn, *lzdai@xmu.edu.cn

Electronic Supplementary Information (ESI) available: Synthesis and NMR spectra, TEM images and XPS Spectra of polymer precursors and Ta-NCAs, Aa-NCa₈₅₀, Ta-NCb₈₅₀. electrochemical assessment of the Ta-NCAs, Aa-NCa₈₅₀, Ta-NCb₈₅₀. See DOI: 10.1039/x0xx00000x

frameworks (COFs) organized by C=N bonds have been adopted as precursors for N-doped carbon materials.²³ Because of its porous structure and electronic conductivity, this type of COFs can be directly used as promising supercapacitor materials without carbonization.²⁴⁻²⁶ Notably, the preparation condition of COFs is normally quite harsh, which needs not only high temperature but also long reaction time and catalyst (120 °C for 3 d in the presence with acetic acid). Schiff-base polymers (SBPs) are another class of promising precursors for N-doped carbon materials. Xue et al. synthesized Schiff-base/resin copolymers under ZnCl₂ medium (160 °C, 8 h), and transformed them into nitrogen-rich porous carbon nanosheets via carbonization.²⁷ Wei et al. synthesized Schiff-base polymers via a mild condition (water bath, 70 °C, 12 h, N₂ protection), then prepared nitrogen-rich porous carbon through the pyrolysis of Schiff-base polymer and ZnCl₂ mixture.²⁸ Apparently, the synthesis of SBPs often requires heating treatment and long reaction time. Besides, the use of ZnCl₂ as template to generate porous structure, can easily lead to tedious post-processing, involving a complicate and irksome template-removal process like acid-etching. Therefore, exploring relatively facile synthetic routes to nitrogen-containing precursors as well as simple carbonization process is of great significance for the development of nitrogen-doped carbon materials.^{1, 29-32}

Herein, we developed a novel synthetic approach to nitrogen-rich Schiff-base polymer (named as Ta-TPA-TAA), therefore fabricating nitrogen-doped porous carbon materials (Ta-NCas) via straightforward carbonization of this polymeric precursor without any template. This tactic has the following advantages: i) the synthetic procedure is facile and highly adaptable. ii) the strategy does not require heating, long reaction time, salt template as well as tedious post-processing such as activation and template-removal process. iii) the as-prepared N-doped carbon materials display hierarchical porous structures, and show excellent supercapacitance performances in both acid and alkaline electrolytes (1 M H₂SO₄ and 6 M KOH electrolytes). This synthetic route may provide possibilities to synthesize other C=N based polymer precursors for high performance carbon materials, by selecting different kinds of amine and aldehyde functionalized monomers. Besides, we investigated the effect of carbonization temperature on specific surface area, nitrogen contents and wettability of Ta-NCas, which can determine on the EDLC capacitance, pseudocapacitance and overall specific capacitance of the Ta-NCas. The finding of EDLC and faradaic capacitance contributions to the overall specific capacitance is crucial for the future fabrication of N-doped carbons in supercapacitors.

Experimental

Materials

Polyvinylidene fluoride (PVDF), terephthalaldehyde (TPA), 1,3,5-tris(4-aminophenyl)benzene (TAB), N-methylpyrrolidone (NMP) were obtained from Aladdin Company. 4-aminobenzonitrile and Trifluoromethanesulfonic acid (Ta) were supplied by J&K Chemical. 1,3,5-trimethylbenzene, 1,4-dioxane,

ethanol, H₂SO₄, acetic acid (Aa), KOH and NH₃·H₂O were purchased from Shanghai Chemical Reagent Industry. All the reagents and solvents were used as received. 2,4,6-Tris(4-aminophenyl)-1,3,5-triazine (TAA) was synthesized according to the previous report with minor modification.³³

Synthesis of Ta-NCas

Typically, 0.709 g of TAA (2 mmol) and 0.40 g of TPA (3 mmol) were taken in a 50 mL round bottom flask and dissolved in 10 mL of 1,3,5-trimethylbenzene, 1,4-dioxane mixed solvents (v : v = 1 : 4). To this solution, 20 μL of trifluoromethanesulfonic acid was added, and precipitate was generated immediately. The reaction mixture was further stirred at room temperature for 10 min and then centrifuged, washed with ethanol for 3 times to remove unreacted monomers and afford solid powder. After drying in vacuum, the as-prepared Ta-TPA-TAA nitrogen-containing precursors were carbonized at Ar atmosphere for 2 h with a heating rate of 5 °C min⁻¹ to prepare Ta-NCas. According to the carbonization temperature, the resultant samples were designated as Ta-NCa₆₅₀, Ta-NCa₇₅₀, Ta-NCa₈₅₀, Ta-NCa₉₅₀. Control samples named as Aa-NCa₈₅₀ and Ta-NCb₈₅₀ were also fabricated, detailed preparation process is exhibited in the supporting information.

Preparation of Working Electrode

The mixture comprising 95% samples (1 mg) and 5% PVDF was added into the NMP, followed by sonication for 30 min to form a uniform slurry. Subsequently, the above uniform slurry was casted onto a glassy carbon electrode polished by alumina and dried at 110 °C for 12 h in vacuum drying oven. The mass loading of active materials in every electrode was about 3.5 mg cm⁻².

Characterizations

Transmission electron microscopy (TEM) images were taken using a JEM2100 instrument at an acceleration voltage of 200 kV. The high-angle annular dark-field scanning transmission electron microscopy (HAADF-STEM) images and the elemental energy-dispersive X-ray spectroscopy (EDX) mapping were acquired on a FEI Talos F200 microscope operated at 300 kV. The X-ray diffraction (XRD) were performed on a Desktop X-ray Diffractometer using Cu (600 W) Kα radiation. The Raman spectra were acquired on Xplora using 638 nm excitation wavelength. The Brunauer-Emmett-Teller (BET) surface area and pore size distribution were measured using an ASAP 2460 system, and all samples were degassed at 120 °C for 24 h under vacuum before measurement. The X-ray photoelectron spectroscopy (XPS) spectra were obtained from a PHI Quantum-2000 photoelectron spectrometer (Al Kα with 1486.6 eV) and all the spectra were calibrated with the C 1s peak at 284.6 eV as an internal standard.

Electrochemical measurements

All electrochemical measurements were measured on an electrochemical workstation (CHI 760E), employing a three-electrode cell and carried out at room temperature. Glassy carbon electrode and Pt foil were used as working electrode and counter electrode, respectively. Hg/HgO (1 M KOH) was used as a reference electrode in 6 M KOH aqueous electrolyte, Hg/HgCl₂ (saturated KCl) was used as a reference electrode in 1 M H₂SO₄

aqueous electrolyte. The specific capacitance of the active materials was calculated by the following formula: $C = It / m\Delta V$, where I , t , m and ΔV stand for the charge/discharge current, the discharging time, the mass of electrode materials and the potential window during charge/discharge, respectively.

Results and discussions

Morphology and composition characterization

TAA with high nitrogen content can react with aldehydes to form imine bonds and has been used as a building block for the construction of COFs and hypercrosslinked porous polymers. Besides, the as-formed C=N bond has a high bond energy (615 kJ mol⁻¹), therefore preventing N element from loss during the carbonization process.³⁴ Starting from TAA and TPA, we synthesized high nitrogen contained crosslinked polymer Ta-TPA-TAA via Schiff-base condensation reaction catalyzed by trifluoromethanesulfonic acid in a 10 min reaction time (Fig. 1). To feature the influence of catalyst on the synthesis of precursor as well as the property of the final carbon materials, the crosslinked polymer was also prepared by using acetic acid as catalyst (denoted as Aa-TPA-TAA, Scheme S1). Notably, we found that the synthesis of Aa-TPA-TAA required more catalyst ($n_{\text{Aa}}:n_{\text{Ta}} \approx 77.5$) and much longer reaction times (detailed synthetic procedure is shown in the supporting information). Through a simple carbonalization procedure, all these precursors were easily transformed into nitrogen doped carbon materials.

The fourier transform infrared spectroscopy (FT-IR) was adopted to characterize the chemical structure of polymer precursors. In the FT-IR spectrum of Ta-TPA-TAA, characteristic peak at ~ 3320 cm⁻¹ derived from N-H as well as the peak at 1686 cm⁻¹ derived from C=O attenuates greatly, while absorption peak at 1578 cm⁻¹ (C=N) appears (Fig. S2a), providing strong evidence for the successful synthesis of Schiff-base polymer Ta-TPA-TAA.^{29,32,35} Aa-TPA-TAA displays a similar FT-IR spectrum, except for a stronger signal of unreacted aldehyde groups caused by the lower catalytic efficiency of acetic acid (Fig. S2a). The element species and contents of TAA, TPA and Ta-TPA-TAA

polymer were confirmed by the XPS spectra (Fig. S2b, Table S1). In the N 1s spectrum of TAA (Fig. S2c), two binding energies centered at 398.3 and 399.4 eV are observed, corresponding to triazine N and NH₂. For the N 1s spectrum of Ta-TPA-TAA shown in Fig. S2d, a new peak at 398.9 eV (C=N bonds) emerges, except for the triazine N peak (398.3 eV) and the evidently decreased NH₂ peak (399.4 eV). These results indicate that the Schiff-base condensation between TAA and TPA occurs, but does not consume all the imine and aldehyde groups.^{5,36,37}

TEM image of Ta-TPA-TAA shown in Fig. S3 displays a analogously spherical shape with diameter of ~ 100 nm and agglomeration particle. After carbonization at different temperatures, the as formed carbon materials Ta-NCas can almost preserve the morphology of Ta-TPA-TAA precursor except for a coarse surface, as characterized by SEM and TEM (Fig. 2a, S3, S4 and S5). High resolution TEM images (Fig. 2b and S4) of Ta-NCas show obvious porosity. Intriguingly, lattice fringes appear when carbonization temperature arrives to 750 °C and become more pronounced with the rising of carbonization temperature, indicating that the carbon matrix of Ta-NCas has more ordered structure at higher carbonization temperature. For Aa-NCa₈₅₀, SEM and TEM images show a jackfruit-shape with a larger size of 200-600 nm and no lattice fringe appears (Fig. S6). Energy-dispersive X-ray (EDX) mapping of Ta-NCa₈₅₀ (Fig. 2c) confirms the presence of elements C, O, N and each element disperses homogeneously in the carbon matrix. This is favorable in increasing the accessible probability of doping atoms, and improving the faradaic pseudocapacitance of heteroatom-doped carbon materials.^{1,38}

The XRD patterns (Fig. 2d) of Ta-NCas show two broad diffraction peaks at 25° and 43°, corresponding to the (002) and (100) lattice planes. This result indicates that a disturbed structure of amorphous carbon, which is beneficial for higher specific surface area, is formed, because of the incorporation of heteroatom in the carbon lattice. Besides, it is worth noting that the location of the diffraction peak of Ta-NCas moves slightly to the high angle, which indicates that the size of condensed aromatic structure in Ta-NCas gradually increases with the increasing of carbonization temperature.^{17,39}

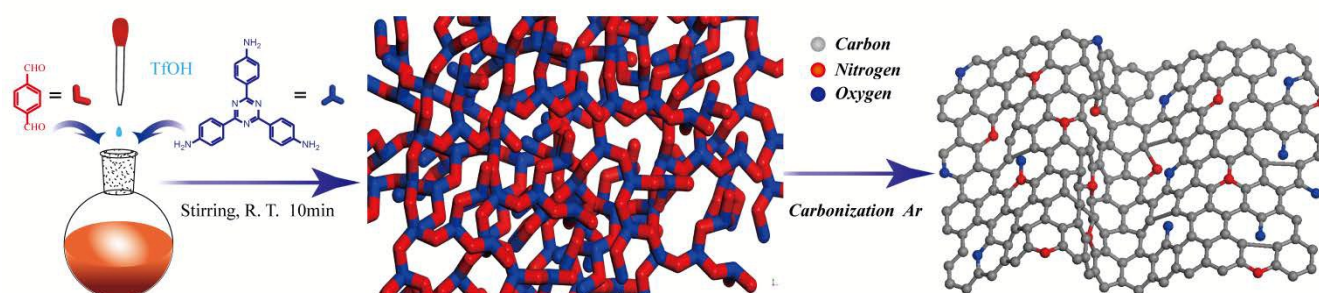


Fig. 1 Synthetic process of Ta-TPA-TAA cross-linked polymer and Ta-NCas.

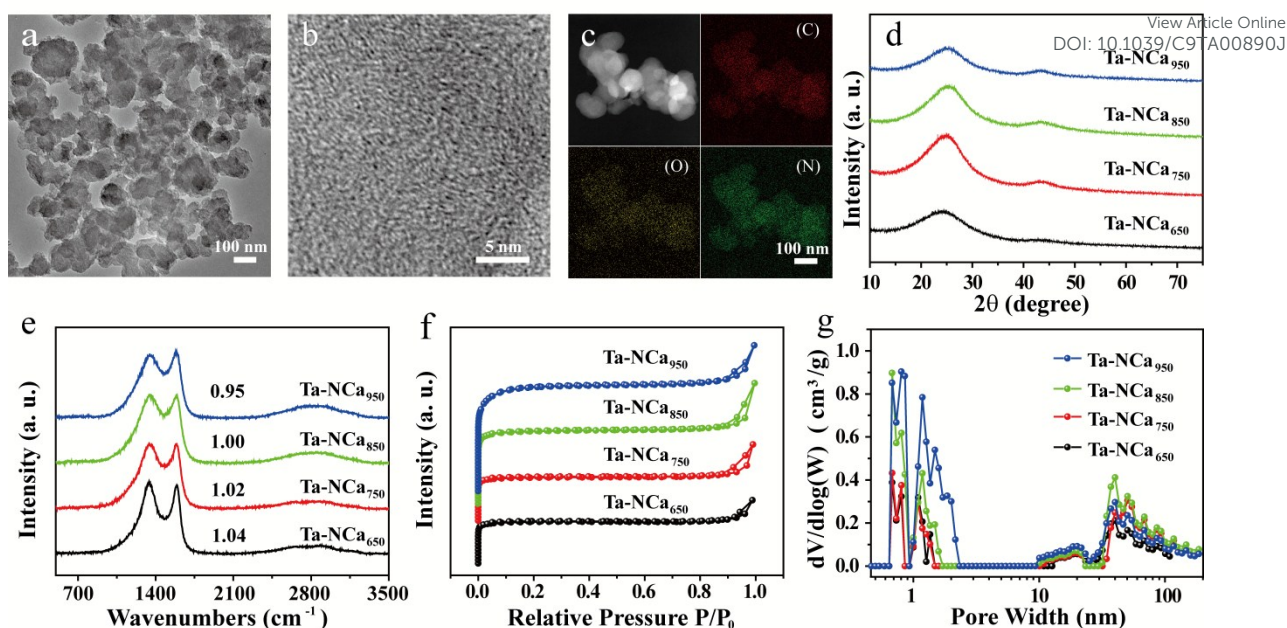


Fig. 2 TEM image of Ta-NCa₈₅₀ (a), high resolution TEM image of Ta-NCa₈₅₀ (b), HAADF-STEM images and EDS element mapping of C, O and N for Ta-NCa₈₅₀ (c); XRD patterns (d), Raman spectra (e), N₂ adsorption/desorption isotherms (f) and the DFT pore size distribution (g) of Ta-NCs.

The Raman spectra depicted in Fig. 2e show two broad bands centered at 1350 and 1586 cm^{-1} , corresponding to the disordered structures and defects (D band), and ordered graphitic structures (G band), respectively.^{40,41} The intensity ratio (I_D/I_G) of carbon-based materials suggests the graphitization degree and the I_D/I_G values of Ta-NCa₆₅₀, Ta-NCa₇₅₀, Ta-NCa₈₅₀ and Ta-NCa₉₅₀ are calculated to be 1.04, 1.02, 1.00, 0.95, respectively. Apparently, the graphitization degree for Ta-NCs gradually increases as the temperature rising from 650 to 950 °C, further suggesting the amorphous structure in Ta-NCs.^{5,42,43} The pore structure and surface area of the resultant samples were evaluated through nitrogen adsorption/desorption measurements at 77 K. All Ta-NCs (Fig. 2f) reveal a fast nitrogen uptake at a relatively low pressure range ($P/P_0 < 0.01$), suggesting that Ta-NCs mainly have narrow micropores (< 2 nm), which is suitable for the diffusion of electrolyte ions by minimizing the molecular diffusion limitation, thus possessing advantage for the enhancement of supercapacitive performance. A further increased uptake of nitrogen is observed at high pressure range ($P/P_0 > 0.9$), indicating the coexistence of both mesopores and macropores. This structure can provide ion-buffering reservoirs to minimize the ionic diffusion distances and facilitate the electrolyte ion transport, therefore leading to an increased electrolyte-accessible surface area. The pore size distribution of the resultant samples depicted in Fig. 2g shows a major peak ranged from 0.7~2 nm together with other two secondary peaks at ~15 and ~50 nm, respectively. Actually, the interconnectivity of the open micro-meso-macropores is convenient for the ion diffusion and adsorption, which is of great importance to supercapacitive performance.^{2,10,12,42,44} Brunauer-Emmett-Teller (BET) surface areas are summarized in Table S2. The surface areas of Ta-NCa₆₅₀, Ta-NCa₇₅₀, Ta-NCa₈₅₀ and Ta-NCa₉₅₀

are 373, 440, 706 to 950 $\text{m}^2 \text{g}^{-1}$, with corresponding total pore volumes of 0.24, 0.29, 0.44 to 0.54 $\text{cm}^3 \text{g}^{-1}$, respectively.^{5,8} Remarkably, the BET surface areas of Ta-NCa₆₅₀ and Ta-NCa₇₅₀ are much lower than that of Ta-NCa₈₅₀ and Ta-NCa₉₅₀. This is because Ta-TPA-TAA polymer has two decomposition stages and the temperatures of the max decomposition rate for each stage appear at 565 and 765 °C respectively (Fig. S7). At carbonization temperatures of 850 and 950 °C, a fierce decomposition occurs, which results in the loss of heteroatom. As indicated by XPS results, the N content decreases from 7.26% at 650 °C to 1.51% at 950 °C and the O content decreases from 8.24% at 650 °C to 3.82% at 950 °C (Table S2). In the case of Aa-NCa₈₅₀, the adsorption/desorption isotherm displays typical I curve, indicating the presence of ample micropores with pore size distribution of 0.5~1.5 nm (Fig. S8, Table S2). The surface area of Aa-NCa₈₅₀ is 722 $\text{m}^2 \text{g}^{-1}$, with corresponding total pore volume of 0.4 $\text{cm}^3 \text{g}^{-1}$.

The composition of the Ta-NCs and Aa-NCa₈₅₀ were characterized by XPS. XPS survey spectra (Fig. 3a and S10) show that Ta-NCs and Aa-NCa₈₅₀ samples comprise C, N and O. Taking Ta-NCa₈₅₀ as an example, the high-resolution C 1s spectrum (Fig. 3b) is divided into three components located at 288.3 ± 0.1 , 285.5 ± 0.1 , 284.8 ± 0.1 eV, which are attributed to C=O, C-N/C-O, C=C/C-C, respectively. The O 1s spectrum (Fig. 3c) reveals two oxygen-based groups: O=C (531.3 ± 0.1 eV), C-O-C/C-OH (532.9 ± 0.1 eV). For the N 1s XPS result of Ta-NC₈₅₀ (Fig. 3d), four distinct N configurations exist, i.e., triazine N (398.3 ± 0.1 eV), pyrrolic N (399.6 ± 0.1 eV), quaternary N (401.1 ± 0.1 eV) and oxidized-N (402.9 ± 0.1 eV).^{4,7,10,45-47} The atomic contents of C, O and N evaluated from the XPS (Fig. 3, S9 and S10) are summarized in Table S2. The absolute and relative atomic contents of N configurations of Ta-NCs versus carbonization temperature are plotted in Fig. S11. Notably, the

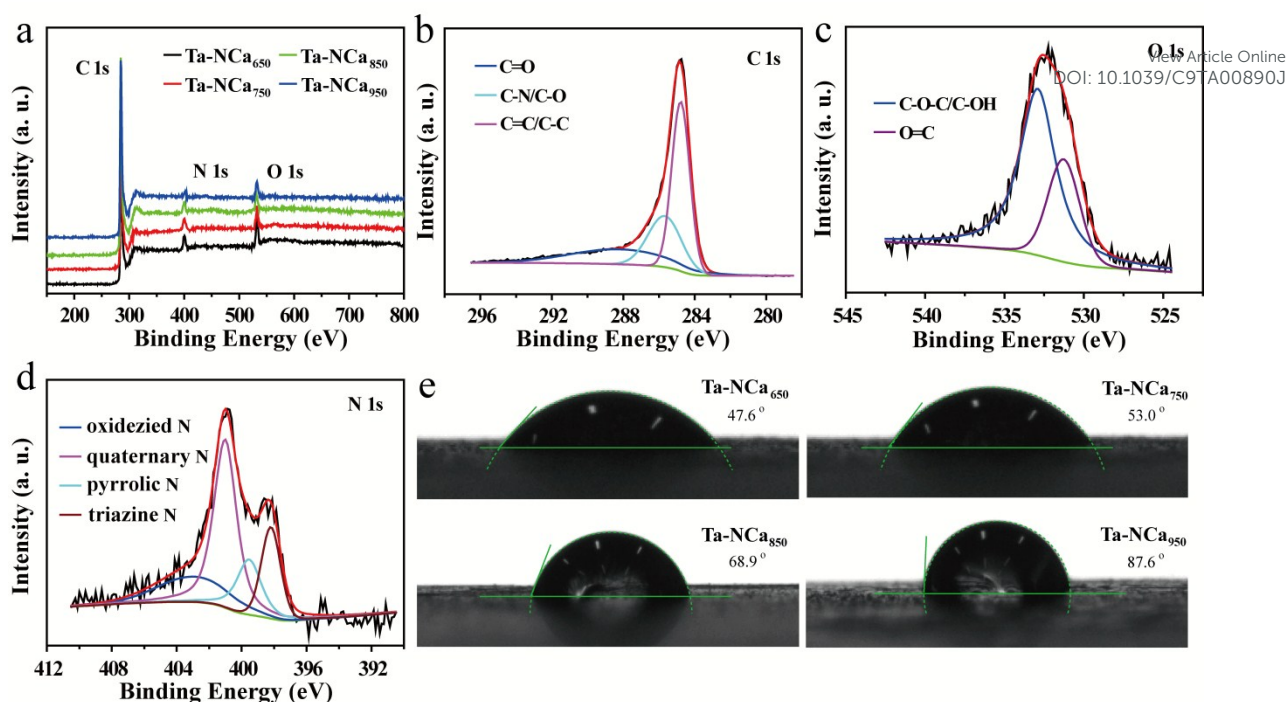


Fig. 3 XPS survey spectra of Ta-NCAs (a); High-resolution XPS spectra of C 1s (b), O 1s (c) and N 1s (d) for Ta-NCa₈₅₀; Measurements of contact angle to 6 M KOH of Ta-NCAs (e).

contents of O, N reduce and the absolute content of triazine N decrease with the increasing of pyrolysis temperature, indicating that triazine frameworks gradually break down. Moreover, an increase of carbonization temperature reduces the relative contents of triazine N and pyrrolic N, but improves the relative contents of quaternary N and oxidized-N. Possibly, the formation of quaternary N and oxidized-N requires a relatively high temperature. The decreased contents of N and O

elements mean the poor wettability of Ta-NCAs electrode toward electrolyte, which is certified by the increased dynamic contact angle of 6 M KOH electrolyte on the Ta-NCAs surface (Fig. 3e and Table S2). From the results of above, we concluded that the temperature greatly affects the pore structure, composition, N-configurations of Ta-NCAs and thus the wettability, all of which finally enable the modulations in the electrochemical performances of Ta-NCAs.

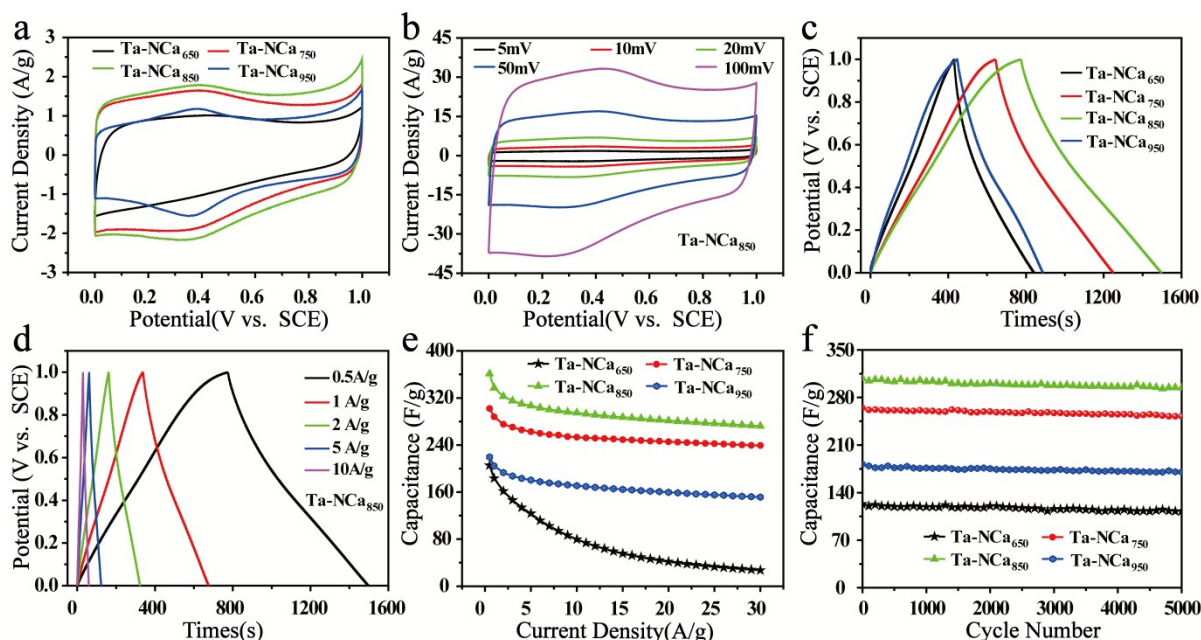


Fig. 4 Electrochemical performance of Ta-NCAs in 1 M H₂SO₄. CV curves of Ta-NCAs at 5 mV s⁻¹ (a); CV curves of Ta-NCa₈₅₀ at the scan rates from 5 to 100 mV s⁻¹ (b); Galvanostatic charge/discharge profiles of Ta-NCAs at 0.5 A g⁻¹ (c); Galvanostatic charge/discharge profiles of Ta-NCa₈₅₀ at the current densities from 0.5 to 10 A g⁻¹ (d); Specific capacitance as a function of different current densities of Ta-NCAs (e); The stability evaluation of Ta-NCAs at 5 A g⁻¹ (f).

Table 1 EDLC and faradaic capacitance contributions to overall capacitance of Ta-NCAs at 0.5 A g⁻¹.

View Article Online

DOI: 10.1039/C9TA00890J

	C, H ₂ SO ₄ ^a			C, KOH ^b		
	C _g (F g ⁻¹)	C _{EDLC} (F g ⁻¹)	C _{Faradaic} (F g ⁻¹)	C _g (F g ⁻¹)	C _{EDLC} (F g ⁻¹)	C _{Faradaic} (F g ⁻¹)
Ta-NCa ₆₅₀	205.5	40.5	165	193	47	146
Ta-NCa ₇₅₀	303	122.5	180.5	308.5	150	158.5
Ta-NCa ₈₅₀	362	162	200	374.5	205.5	169
Ta-NCa ₉₅₀	220	98	122	157	100	57

Capacitance obtained from galvanostatic charge discharge curves of Ta-NCAs at 0.5 A g⁻¹ in 1 M H₂SO₄^a and in 6 M KOH^b.**Electrochemical characterization**

To evaluate the electrochemical performance of Ta-NCAs, cyclic voltammetry (CV) curves were recorded using a conventional three-electrode system in both 1 M H₂SO₄ (Fig. 4a) and 6 M KOH (Fig. 5a) aqueous electrolytes. CV curves at scan rate of 5 mV s⁻¹ display a quasi-rectangular shape, implying an ideal capacitive performance. Steep slopes of the current change at the switching potential can also be observed to the CV curves, which manifests the low mass-transfer resistance.^{2,42} With the increase of the scan rates from 5 to 100 mV s⁻¹, the current density increases significantly. The CV curves of Ta-NCa₇₅₀, Ta-NCa₈₅₀ and Ta-NCa₉₅₀ can retain the quasi-rectangular shape well except for that of Ta-NCa₆₅₀, as its CV curve gradually changes into a fusiform shape (Fig. 4b, 5b, S12 and S16). Therefore, Ta-NCAs prepared from temperatures of 750, 850 and 950 °C have more excellent rate capability than that derived from 650 °C. Additionally, obvious broad redox peaks ranged from 0.1 to 0.5 V (vs. Hg/Hg₂Cl₂) are discerned in 1 M H₂SO₄ aqueous electrolyte, and a gradual current increasing at around -0.6 V (vs. Hg/HgO) in 6 M KOH aqueous electrolyte

can be observed. These are related to pseudocapacitance contributed from the redox reactions of the pyrrolic N, pyridinic N, and oxygen-containing functionalities. It can also be noted that among all the samples, Ta-NCa₈₅₀ has the largest area of CV curve, implying that Ta-NCa₈₅₀ has better capacitive performance than other samples. With regard to the contrast sample, Aa-NCa₈₅₀ displays similar CV curves. However, the areas of its CV curves are much smaller by comparing with Ta-NCa₈₅₀ in both 1 M H₂SO₄ (Fig. S13a) and 6 M KOH (Fig. S13d) electrolytes, indicating a non-ideal capacitance performance. Indeed, Aa-NCa₈₅₀ derived from Aa-TPA-TAA reveals a worse capacitance performance in comparison with Ta-NCa₈₅₀ derived from Ta-TPA-TAA, as the specific capacitances of Aa-NCa₈₅₀ are 214 F g⁻¹ in 1 M H₂SO₄ (Fig. S13b) and 230 F g⁻¹ in 6 M KOH (Fig. S13e) at 0.5 A g⁻¹. This may be caused by the lack of mesopore and macropore structures, because of the lower catalytic efficiency of acetic acid.

The capacitance evolution trend of Ta-NCAs versus carbonization temperature is consistent with the CV results. At a current density of 0.5 A g⁻¹, the specific capacitances of Ta-

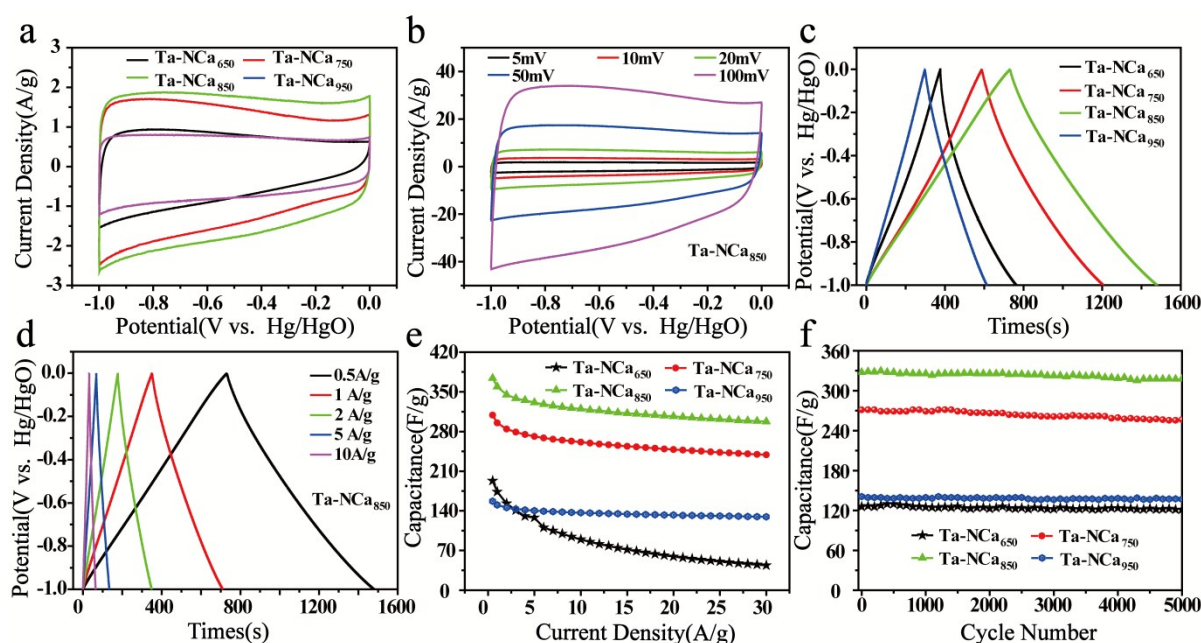


Fig. 5 Electrochemical performance of Ta-NCAs in 6 M KOH. CV curves of Ta-NCAs at 5 mV s⁻¹ (a); CV curves of Ta-NCa₈₅₀ at the scan rates from 5 to 100 mV s⁻¹ (b); Galvanostatic charge discharge profiles of Ta-NCAs at 0.5 A g⁻¹ (c); Galvanostatic charge discharge profiles of Ta-NCa₈₅₀ at the current densities from 0.5 to 10 A g⁻¹ (d); Specific capacitance as a function of different current densities of Ta-NCAs (e); The stability evaluation of Ta-NCAs at 5 A g⁻¹ (f).

NCa₆₅₀, Ta-NCa₇₅₀, Ta-NCa₈₅₀ and Ta-NCa₉₅₀ are 205.5, 303, 362, 220 F g⁻¹ in 1 M H₂SO₄, and 193, 308.5, 374.5, 157 F g⁻¹ in 6 M KOH, respectively, which is superior or comparable to that of previous reports (Table S3). Apparently, 850 °C of carbonization temperature results in the formation of Ta-NCas with the highest capacitance. Notably, the representative CD curves of Ta-NCas at 0.5 A g⁻¹ display near triangle shapes with deviation in both acid (Fig. 4c) and basic media (Fig. 5c), suggesting the coexistence of EDLC capacitance and faradaic capacitance. To estimate the EDLC and faradaic capacitance contributions, the overall specific capacitance is divided into two parts by the differing slopes of the discharge portion (Fig. S15 and S18), and the detailed results are listed in Table 1.^{7,48,49} Indeed, Ta-NCas show remarkably lower EDLC performance in H₂SO₄ when comparing with that of in 6 M KOH, as the capacitances are 40.5, 122.5, 162 and 98 F g⁻¹ versus 47, 150, 205.5 and 100 F g⁻¹, respectively. This result can be attributed to two factors: i) the concentration of both K⁺ and OH⁻ is higher than that of H₃O⁺ and SO₄²⁻ (H₂O)₁₂, leading to more electroadsorbed possibilities on the pores; ii) the ionic size of OH⁻ (2.74 Å) is smaller than that of SO₄²⁻ (H₂O)₁₂ (5.33 Å), thus resulting in difficulties of SO₄²⁻ (H₂O)₁₂ ions in penetrating and adsorbing in the narrow micropores.⁵⁰⁻⁵² Hence, double-layer contribution of Ta-NCas to the overall capacitance in H₂SO₄ is lower than that in KOH. Conversely, the faradaic capacitances of Ta-NCas in H₂SO₄ are more significant in comparison with that in 6 M KOH aqueous electrolyte, which can be ascribed to the faradaic interactions between H₃O⁺ and the nitrogen, oxygen-containing functionalities are stronger than those of K⁺, which is consistent with the previous reports.^{53,54}

Since Ta-NCa₆₅₀ possesses a high heteroatom content, a significant faradaic capacitance contribution can be expected. Also, excellent EDLC capacitance is expectable for Ta-NCa₉₅₀ because of its high surface area. However, Ta-NCa₈₅₀ with moderate contents of nitrogen, oxygen and BET surface area shows the favorable EDLC capacitance and faradaic capacitance. This can be explained by synergistic effect of surface wettability, BET area, content of heteroatom. More specifically, the faradaic capacitance is associated with content of heteroatom and the available utilization of heteroatom. The EDLC capacitance is related to the BET surface area and surface wettability. Under 850 °C carbonization temperature, the content of heteroatom and the wettability decrease, but the BET surface area increases from 373 to 706 cm³ g⁻¹ simultaneously, which contribute to the significant improvement of availability of heteroatom. For sample obtained from temperature above 850 °C, the BET surface area continue increases, whereas a large loss of heteroatom occurs. The lower heteroatom content leads to the decrease of surface wettability of Ta-NCa₉₅₀, as evidenced by the contact angle shown in Fig. 3e and Table S2. This is disadvantage for electrolyte ion transport crossing the electrical double layer, thus making more inner surface ion inaccessible. Consequently, it can be concluded that the favorable faradaic capacitance, EDLC performances of Ta-NCa₈₅₀ are attributed to a synergy of the N and O content both on the surface and in the bulk and the surface area.

For practical application, good rate capability and long cycling stability are key parameters for supercapacitors. Chronopotentiometry (CP) curves at different current densities (0.5-30 A g⁻¹) are recorded in 1 M H₂SO₄ (Fig. 4d, S12 and S14) and 6 M KOH (Fig. 5d, S16 and S17), respectively. Calculated by the galvanostatic CD curves, the specific capacitances of Ta-NCa₆₅₀, Ta-NCa₇₅₀, Ta-NCa₈₅₀ and Ta-NCa₉₅₀ at 0.5 A g⁻¹ are 205.5, 303, 362 and 220 F g⁻¹ in H₂SO₄, and 193, 308.5, 374.5 and 157 F g⁻¹ in KOH. At a high current of 30 A g⁻¹, Ta-NCas have specific capacitances of 27.21, 239.1, 272.3 and 151.5 F g⁻¹ in H₂SO₄ (Fig. 4e) and 43.65, 238.8, 297.3 and 129.6 F g⁻¹ in KOH (Fig. 5e). Apparently, except for Ta-NCa₆₅₀, Ta-NCas have a strong endurance at a large current and a good rate capability. After charge and discharge for 5000 cycles at 5 A g⁻¹, the specific capacitances of Ta-NCas reduce unconspicuously in both acid (retention of 96%, Fig. 4f) and basic electrolyte (retention of 94%, Fig. 5f), demonstrating the good cycle stability. Additionally, the stability of electrode film was confirmed by the morphology of the Ta-Nca electrodes shown in the SEM images (Fig. S19). A film with ~91 μm thickness is attached on the glassy carbon electrode, and no morphology or thickness changes can be observed after charge and discharge for 5000 cycles. To further get a deep insight into the electrochemical performance of Ta-NCas, electrochemical impedance spectra (EIS) was conducted (Fig. S20). Obviously, Ta-NCa₈₅₀ displays a smaller semicircle at the high frequency region and a steeper line in low frequency in contrast with other samples, implying a smaller charge-transfer resistance and a faster ionic diffusion, which is kept pace with higher specific capacitance.^{55,56}

Adaptability of the precursor synthetic route

Finally, the high adaptability of our strategy is demonstrated by the extension of building blocks. By using an alternative amine monomer TAB, another C=N based polymer (Ta-TPA-TAB, Scheme S2) was successfully synthesized (as confirmed by FT-IR spectra shown in Fig. S21). Unlike TA-TPA-TAA, TA-TPA-TAB shows hand-like and analogously spherical geometry, which may be caused by the different chemical reactivities.

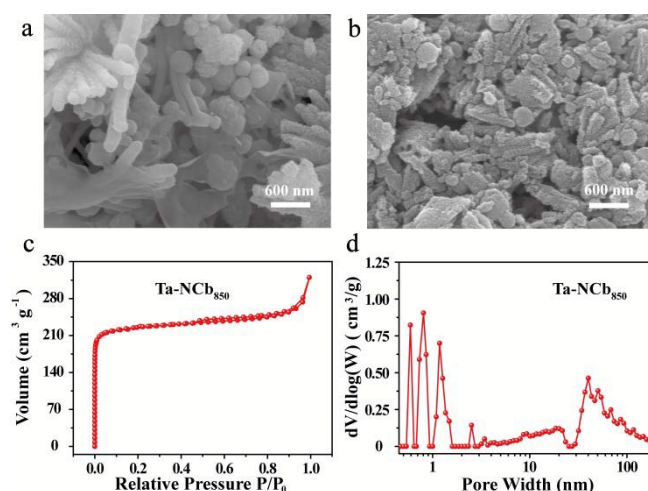


Fig. 6 SEM images of TA-TPA-TAB polymer (a) and Ta-NCb₈₅₀ (b); N₂ adsorption/desorption isotherms (c) and the DFT pore size distribution (d) of Ta-NCb₈₅₀.

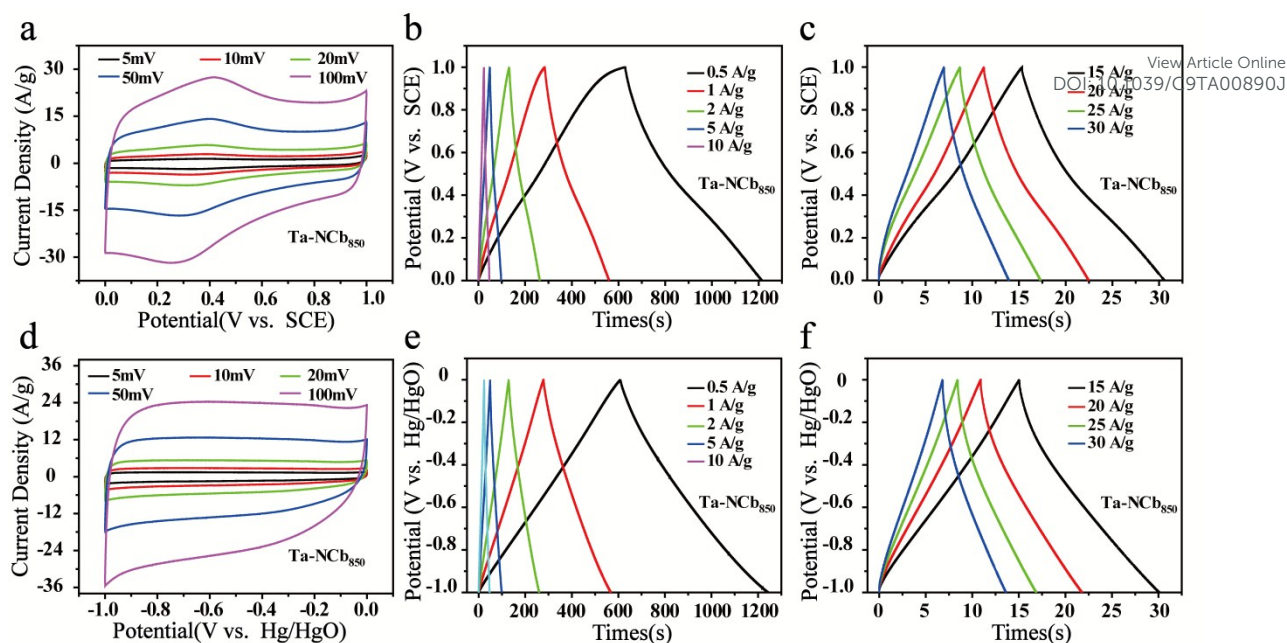


Fig. 7 CV curves of Ta-NCb₈₅₀ at the scan rates from 5 to 100 mV s⁻¹ in 1 M H₂SO₄ (a); Galvanostatic charge discharge profiles of Ta-NCb₈₅₀ at the current densities from 0.5 to 30 A g⁻¹ in 1 M H₂SO₄ (b and c); CV curves of Ta-NCb₈₅₀ at the scan rates from 5 to 100 mV s⁻¹ in 6 M KOH (d); Galvanostatic charge discharge profiles of Ta-NCb₈₅₀ at the current densities from 0.5 to 30 A g⁻¹ in 6 M KOH (e and f).

After carbonization at 850 °C, we obtained carbon material Ta-NCb₈₅₀, which can preserve the morphology of its precursor (Fig. 6). Comparing with Ta-NCa₈₅₀, Ta-NCb₈₅₀ exhibits analogous micro-meso-macropores structure and a higher BET area of 896 m² g⁻¹. XPS analysis indicates that Ta-NCb₈₅₀ has lower N content than that of Ta-NCa₈₅₀ (Fig. S22 and Table 2). CV and CD curves were also acquired for Ta-NCb₈₅₀ in both 1 M H₂SO₄ and 6 M KOH electrolytes (Fig. 7). As can be seen, the CV curves show quasi-rectangular shape and remains unchanged with the scan rates varying from 5 to 100 mV s⁻¹. The CD profiles display near triangle shapes with deviation and the specific capacitances of Ta-NCb₈₅₀ are 296 F g⁻¹ in 1 M H₂SO₄ and 310 F g⁻¹ in 6 M KOH at 0.5 A g⁻¹.

Conclusions

Through a simple reaction between amine and aldehyde, crosslinked polymer precursors possessing high nitrogen content were rapidly and easily synthesized by using trifluoromethanesulfonic acid as catalyst. Pyrolysis treatment of the precursor led to the formation nitrogen-doped carbon materials with hierarchical porous structures, which demonstrated outstanding supercapacitance performances in both acid and alkaline electrolytes. The as prepared carbon material derived from 850 °C carbonization temperature with moderate SSA of 706 m² g⁻¹, contact angle of 68.9° and nitrogen content of 4.39% delivers high capacitances of 362 F g⁻¹ in acidic medium and 374.5 F g⁻¹ in alkaline medium at 0.5 A g⁻¹, which are much higher than that of Aa-NCa₈₅₀ derived from Aa-TPA-TAA synthesized by using acetic acid as catalyst, as the specific capacitances of Aa-NCa₈₅₀ are 214 F g⁻¹ in 1 M H₂SO₄ and 230 F g⁻¹ in 6 M KOH at 0.5 A g⁻¹. This work implies that various C=N based polymer precursor may be easily fabricated by selecting different kinds of amine and aldehyde building blocks, thus

providing possibilities to develop new electrode materials in the field of supercapacitors.

Conflicts of interest

There are no conflicts to declare.

Acknowledgements

This work was supported by the National Natural Science Foundation of China (51673161, 51773172, U1805253); Scientific and Technological Innovation Platform of Fujian Province (2014H2016); Science and Technology Major Project of the Fujian Province (2018HZ0001-1); Xiamen Science and Technology Project (3502Z20183014, 3502Z20183001).

Notes and references

1. L. Hao, X. L. Li and L. J. Zhi, *Adv. Mater.*, 2013, **25**, 3899-3904.
2. Y. G. Wang, Y. F. Song and Y. Y. Xia, *Chem. Soc. Rev.*, 2016, **45**, 5925-5950.
3. T. Ogoshi, K. Yoshikoshi, R. Suetto, H. Nishihara and T. Yamagishi, *Angew. Chem., Int. Ed.*, 2015, **54**, 6466-6469.
4. C. C. Su, C. J. Pei, B. X. Wu, J. F. Qian and Y. W. Tan, *Small*, 2017, **13**, 1700834.
5. Y. J. Li, S. H. Zheng, X. Liu, P. Li, L. Sun, R. X. Yang, S. Wang, Z. S. Wu, X. H. Bao and W. Q. Deng, *Angew. Chem.*, 2018, **130**, 8124-81286.
6. Z. Li, Z. W. Xu, X. H. Tan, H. L. Wang, C. M. B. Holt, T. Stephenson, B. C. Olsen and D. Mitlin, *Energy Environ. Sci.*, 2013, **6**, 871-878.
7. Z. Li, Z. W. Xu, H. L. Wang, J. Ding, B. Zahiri, C. M. B. Holt, X. H. Tan and D. Mitlin, *Energy Environ. Sci.*, 2014, **7**, 1708-1718.

- 8 L. Hao, J. Ning, B. Luo, B. Wang, Y. B. Zhang, Z. H. Tang, J. H. Yang, A. Thomas and L. J. Zhi, *J. Am. Chem. Soc.*, 2015, **137**, 219-225.
- 9 T. Q. Lin, I. W. Chen, F. X. Liu, C. Y. Yang, H. Bi, F. F. Xu and F. Q. Huang, *Science*, 2015, **350**, 1508-1513.
- 10 J. Li, N. Wang, J. R. Tian, W. Z. Qian and W. Chu, *Adv. Funct. Mater.*, 2018, **28**, 1806153.
- 11 Q. Wang, B. Qin, X. H. Zhang, X. L. Xie, L. Jin and Q. Cao, *J. Mater. Chem. A*, 2018, **6**, 19653-19663.
- 12 S. Dutta, A. Bhaumik and K. C. W. Wu, *Energy Environ. Sci.*, 2014, **7**, 3574-3592.
- 13 L. Hao, B. Luo, X. L. Li, M. H. Jin, Y. Fang, Z. H. Tang, Y. Y. Jia, M. H. Liang, A. Thomas, J. H. Yang and L. J. Zhi, *Energy Environ. Sci.*, 2012, **5**, 9747-9751.
- 14 Z. Ling, G. Wang, M. Zhang, X. Fan, C. Yu, J. Yang, N. Xiao and J. Qiu, *Nanoscale*, 2015, **7**, 5120-5125.
- 15 C. L. Mangun, K. R. Benak, J. Economy and K. L. Foster, *Carbon*, 2001, **39**, 1809-1820.
- 16 B. Krüner, A. Schreiber, A. Tolosa, A. Quade, F. Badaczewski, T. Pfaff, B. M. Smarsly and V. Presser, *Carbon*, 2018, **132**, 220-231.
- 17 M. Widmaier, B. Krüner, N. Jackel, M. Aslan, S. Fleischmann, C. Engel and V. Presser, *J. Electrochem. Soc.*, 2016, **163**, A2956-A2964.
- 18 X. L. Zhang, L. Ma, M. Y. Gan, G. Fu, M. Jin, Y. Lei, P. S. Yang and M. F. Yan, *J. Power Sources*, 2017, **340**, 22-31.
- 19 L. F. Chen, X. D. Zhang, H. W. Liang, M. Kong, Q. F. Guan, P. Chen, Z. Y. Wu and S. H. Yu, *ACS Nano*, 2012, **6**, 7092-7102.
- 20 G. X. Xin, M. M. Wang, W. H. Zhang, J. L. Song and B. W. Zhang, *Electrochim. Acta*, 2018, **291**, 168-176.
- 21 L. F. Chen, Y. Lu, L. Yu and X. W. Lou, *Energy Environ. Sci.*, 2017, **10**, 1777-1783.
- 22 M. J. Zhong, E. K. Kim, J. P. McGann, S. E. Chun, J. F. Whitacre, M. Jaroniec, K. Matyjaszewski and T. Kowalewski, *J. Am. Chem. Soc.*, 2012, **134**, 14846-14857.
- 23 Y. H. Zhao, M. X. Liu, X. X. Deng, L. Miao, P. K. Tripathi, X. M. Ma, D. Z. Zhu, Z. J. Xu, Z. X. Hao and L. H. Gan, *Electrochim. Acta*, 2015, **153**, 448-455.
- 24 P. Bhanja, S. K. Das, K. Bhunia, D. Pradhan, T. Hayashi, Y. Hijikata, S. Irle and A. Bhaumik, *ACS Sustainable Chem. Eng.*, 2018, **6**, 202-209.
- 25 B. C. Patra, S. Khilari, L. Satyanarayana, D. Pradhan and A. Bhaumik, *Chem. Commun.*, 2016, **52**, 7592-7595.
- 26 P. Bhanja, K. Bhunia, S. K. Das, D. Pradhan, R. Kimura, Y. Hijikata, S. Irle and A. Bhaumik, *ChemSusChem*, 2017, **10**, 921-929.
- 27 D. F. Xue, D. Z. Zhu, M. X. Liu, H. Duan, L. C. Li, X. L. Chai, Z. W. Wang, Y. K. Lv, W. Xiong and L. H. Gan, *ACS Appl. Nano Mater.*, 2018, **1**, 4998-5007.
- 28 J. S. Wei, H. Ding, Y. G. Wang and H. M. Xiong, *ACS Appl. Mater. Interfaces*, 2015, **7**, 5811-5819.
- 29 H. T. Wei, J. Ning, X. D. Cao, X. H. Li and L. Hao, *J. Am. Chem. Soc.*, 2018, **140**, 11618-11622.
- 30 E. L. Spitler and William R. Dichtel, *Nat. Chem.*, 2010, **2**, 672-677.
- 31 M. Baroncini, S. d'Agostino, G. Bergamini, P. Ceroni, A. Comotti, P. Sozzani, I. Bassanetti, F. Grepioni, T. M. Hernandez, S. Silvi, M. Venturi and A. Credi, *Nat. Chem.*, 2015, **7**, 634-640.
- 32 Y. Z. Liu, Y. H. Ma, Y. B. Zhao, X. X. Sun, F. Gándara, H. Furukawa, Z. Liu, H. Y. Zhu, C. H. Zhu, K. Suenaga, P. Oleynikov, A. S. Alshammari, X. Zhang, O. Terasaki and O. M. Yaghi, *Science*, 2016, **351**, 365-369.
- 33 S. H. Xiong, J. Tao, Y. Y. Wang, J. T. Tang, C. Liu, Q. Q. Liu, Y. Wang, G. P. Yu and C. Y. Pan, *Chem. Commun.*, 2018, **54**, 8450-8453.
- 34 D. Z. Zhu, J. X. Jiang, D. M. Sun, X. Y. Qian, Y. W. Wang, L. C. Li, Z. W. Wang, X. L. Chai, L. H. Gan and M. X. Liu, *J. Mater. Chem. A*, 2018, **6**, 12334-12343.
- 35 Y. W. Peng, W. K. Wong, Z. G. Hu, Y. D. Cheng, D. Q. Yuan, S. A. Khan and D. Zhao, *Chem. Mater.*, 2016, **4**, 5095-5101.
- 36 B. J. Lindberg and J. Hedman, *Chem. Scr.*, 1975, **7**, 155-166.
- 37 C. H. Yuan, T. Wu, J. Mao, T. Chen, Y. T. Li, M. Li, Y. T. Xu, B. R. Zeng, W. A. Luo, L. K. Yu, G. F. Zheng and L. Z. Dai, *J. Am. Chem. Soc.*, 2018, **140**, 7629-7636.
- 38 L. Dai, Y. Xue, L. Qu, H. J. Choi and J. B. Baek, *Chem. Rev.*, 2015, **115**, 4823-4892.
- 39 J. H. Kim, M. Byeon, Y. C. Jeong, J. Lee, H. I. Cho, Y. E. Shin, S. J. Yang and C. R. Park, *Carbon*, 2018, **140**, 68-76.
- 40 J. Schwan, S. Ulrich, V. Batori, and H. Ehrhardt, *J. Appl. Phys.*, 1996, **80**, 440-447.
- 41 K. Takai, M. Oga, H. Sato, and T. Enoki, *Phys. Rev. B*, 2003, **67**, 214202.
- 42 Y. Q. Zhao, M. Lu, P. Y. Tao, Y. J. Zhang, X. T. Gong, Z. Yang, G. Q. Zhang and H. L. Li, *J. Power Sources*, 2016, **307**, 391-400.
- 43 L. Miao, D. Zhu, M. Liu, H. Duan, Z. Wang, Y. Lv, W. Xiong, Q. Zhu, L. Li, X. Chai and L. Gan, *Chem. Eng. J.*, 2018, **347**, 233-242.
- 44 J. Zhao, Y. F. Jiang, H. Fan, M. Liu, O. Zhuo, X. Z. Wang, Q. Wu, L. J. Yang, Y. W. Ma and Z. Hu, *Adv. Mater.*, 2017, **29**, 1604569.
- 45 B. D. Hulicova-Jurcakova, M. Seredych, G. Q. Lu and T. J. Bandoz, *Adv. Funct. Mater.*, 2009, **19**, 438-447.
- 46 D. Marton, K. J. Boyd, A. H. Al-Bayati, S. S. Todorov and J. W. Rabalais, *Phys. Rev. Lett.*, 1994, **73**, 118-121.
- 47 M. Zhou, X. Y. Li, H. Zhao, J. Wang, Y. P. Zhao, F. Y. Gea and Z. S. Cai, *J. Mater. Chem. A*, 2018, **6**, 1621-1629.
- 48 Y. Chang, C. H. Yuan, C. Liu, J. Mao, Y. T. Li, H. Y. Wu, Y. Z. Wu, Y. T. Xu, B. R. Zeng and L. Z. Dai, *J. Power Sources*, 2017, **365**, 354-361.
- 49 Z. Y. Lin, Y. Liu, Y. G. Yao, O. J. Hildreth, Z. Li, K. Moon and C. P. Wong, *J. Phys. Chem. C*, 2011, **115**, 7120-7125.
- 50 D. Hulicova, M. Kodama and H. Hatori, *Chem. Mater.*, 2006, **18**, 2318-2326.
- 51 M. Endo, T. Maeda, T. Takeda, Y. J. Kim, K. Koshiba, H. Hara and M. S. Dresselhaus, *J. Electrochem. Soc.*, 2001, **148**, A910-A914.
- 52 J. Chmiola, G. Yushin, Y. Gogotsi, C. Portet, P. Simon and P. L. Taberna, *Science*, 2006, **313**, 1760-1763.
- 53 Y. H. Lee, K. H. Chang and C. C. Hu, *J. Power Sources*, 2013, **227**, 300-308.
- 54 B. Ding, D. Guo, Y. H. Wang, X. L. Wu and Z. J. Fan, *J. Power Sources*, 2018, **398**, 113-119.
- 55 S. Zhang and N. Pan, *Adv. Energy Mater.*, 2015, **5**, 1401401.
- 56 A. Eftekhari, *J. Mater. Chem. A*, 2018, **6**, 2866-2876.